magnetism

MDPI

Article

Design and Investigation of a High-Torque-Performance Spoke-Type Flux-Modulated Permanent Magnet Motor

Qian Liu [1], Zixuan Xiang [2,*] and Kunhua Chen [2]

[1] School of Physics and Electronic Engineering, Jiangsu University, Zhenjiang 212013, China; lqxyd@ujs.edu.cn
[2] School of Electrical and Information Engineering, Jiangsu University, Zhenjiang 212013, China; chenkunhua@itjiyi.com
* Correspondence: zxxiang@ujs.edu.cn

Abstract

In this paper, a spoke-type flux-modulated permanent magnet in-wheel (SFM-PMIW) motor is taken as the research object. A design and optimization method for field-modulated motors guided by multi-air-gap harmonics is proposed. In the research, the requirements for high torque and low torque ripple are integrated into the motor design, leading to the implementation of rotor slotting. Subsequently, the influence of rotor slotting on rotor permanent magnet magnetomotive force and rotor permeance is analyzed. Then, by designing the unique modulation behavior after rotor slotting, the air-gap harmonics are altered to improve motor performance, including cogging torque. Guided by this concept, the air-gap harmonics related to cogging torque are analyzed, and these harmonics are used as a design link for motor parameter optimization, resulting in the final motor structure. Finally, a comparative analysis of the no-load and load performance before and after harmonic design is conducted, demonstrating the effectiveness of the proposed design and optimization approach.

Keywords: flux-modulated; permanent magnet motor; high torque; low torque ripple; harmonic

1. Introduction

Utilizing in-wheel motors as the power source for distributed drive electric vehicles offers advantages such as compact structure, diverse driving modes, and high transmission efficiency [1–4]. Faced with complex operating conditions like frequent start–stop, hill climbing, and high-speed cruising, the drive motor must meet performance requirements including high torque density, high reliability, and high efficiency [5,6]. Permanent magnet synchronous motors (PMSMs) possess merits like high efficiency, the ability to deliver full-load torque even at low speeds, a wide speed regulation range, low output torque ripple, and reduced vibration and noise [7,8]. These characteristics allow PMSMs to meet the various drive demands of distributed drive electric vehicles, making them the primary type currently adopted for in-wheel motors. Delving deeper into the potential of PMSMs regarding comprehensive performance, as represented by torque performance, is a key focus in current drive motor research.

Centering on the three core elements of motors—the PM excitation source, the modulator, and the armature winding—research has been conducted on the design of field-modulated motors [9]. Efficient design of the PM source, including the arrangement, material, and dimensions of the PMs, is a crucial pathway to achieving high torque performance in field-modulated motors [10]. Regarding PM arrangements, a spoke-type PM

Check for updates

Academic Editors: Antonio Orlandi and Jianguo Zhu

Received: 3 June 2026
Revised: 2 October 2026
Accepted: 24 October 2026
Published: 27 October 2026

Copyright: © 2026 by the authors. Licensee MDPI, Basel, Switzerland. This article is an open access article distributed under the terms and conditions of the Creative Commons Attribution (CC BY) license.

arrangement is proposed, which exhibits a stronger flux-focusing effect, effectively enhancing the torque density [11]. In [12], focusing on an irregular PM field-modulated motor directly established connections between air-gap harmonics and PM parameters as well as torque performance. This optimization scheme successfully increases the motor output torque while suppressing torque ripple. In [13], the permanent magnets are designed in an alternate-pole structure. Research indicates that this design allows the back electromotive force and torque density to remain comparable to those of conventional structures while using 40% less PM material.

The modulator plays a role in field modulation within the operational mechanism of field-modulated motors and is key to generating rich air-gap harmonics [14]. Reasonable design of the modulator will directly improve the distribution of air-gap flux density harmonics, thereby enhancing motor performance. In [15,16], several split-tooth schemes for the stator structure are proposed, and various arrangements between stator teeth and fault-tolerant teeth are investigated. The results show that fault-tolerant teeth not only provide fault protection but also exert a positive field modulation effect on the air-gap magnetic field.

Thus, it is evident that whether it is the permanent magnet source, the modulator, or the armature winding, they are all closely linked to the generation mechanism of rich flux density harmonics in the air-gap [17]. Simultaneously, air-gap harmonics are directly related to the performance characteristics, with different harmonics playing distinct roles in motor performance [18]. Starting from the perspective of the air-gap magnetic field in field-modulated motors, analyzing and studying the relationship between multiple air-gap harmonics and motor performance provides a highly beneficial perspective for motor design and optimization [19].

Based on the field modulation mechanism, this paper proposes a design and optimization method for field-modulated motors centered on multiple air-gap harmonics, designing a high-torque-density, high-efficiency spoke-type field-modulated permanent magnet in-wheel motor. The specific chapter contents are as follows. Section 2 primarily elucidates the structure of the SFM-PMIW motor. In Section 3, the operational principle of the SFM-PMIW motor is analyzed from the perspective of air-gap harmonics. Starting with a traditional spoke-type field-modulated motor, it analyzes the characteristics of air-gap harmonics generated by the permanent magnet magnetomotive force, and those generated by the armature winding after slotting are introduced in the rotor of the SFM-PMIW motor. Based on this, the intrinsic relationships between the air-gap harmonics of the SFM-PMIW motor and its output torque and torque ripple are derived. In Section 4, building upon the initial topological design of the motor, we conduct motor optimization through sensitivity analysis and response surface methodology, focusing on optimizing air-gap harmonics to improve the torque performance.

2. Theoretical Analysis and Motor Structure

2.1. Discussion of Pole–Slot Combinations of the PMVW Motor

This paper presents a spoke-type flux-modulated permanent magnet in-wheel (SFM-PMIW) motor with high torque performance characteristics. The motor topology is divided into an outer rotor and a stator. On the outer rotor, PMs are embedded, and the pole pairs are P_r; the stator teeth act as modulation operators, not only modulating the permanent magnetic source on the outer rotor, but also modulating the armature magnetic source. The number of such stator teeth is N_s. In order to achieve a higher transmission ratio, under the condition of limited rotor space, the number of pole pairs of the armature winding should be as small as possible. The combination of P_r and N_s will jointly affect the winding coefficient and the cogging torque of the motor. Specifically, the larger the least common

multiple of P_r and N_s, the smaller the cogging effect of the motor will be. For other sizes, considering the space limitations and manufacturing feasibility, and considering that the difference between the number of PM pole pairs and the number of stator slots cannot be too large, certain constraints need to be imposed on the combination of P_r and N_s.

For three-phase motors, if the number of stator slots is odd, it may cause significant unbalanced magnetic forces during operation, which could lead to some potential mechanical problems after long-term operation. Therefore, the number of slots of the motor is set to be a multiple of six. The following are various mathematical constraint expressions for the pole–slot combinations of the motor:

$$\begin{cases} \mathrm{N}_s = 6r(r = 1, 2, 3 \ldots) \\ [P_r, N_s] > 100 \\ \tau \leq 2 \\ K_d \geq 0.866 \\ P_r < N_s < 2P_r \end{cases} \tag{1}$$

where τ is the span of the winding. The larger the value of τ, the greater the number of stator teeth that each phase and each winding spans. As a result, the end of each phase winding will be larger. This not only leads to a larger winding copper loss, reducing the efficiency of the motor, but also results in a larger inductive reactance, causing a decrease in the motor's power factor. When $\tau = 1$, it indicates that the winding method of the motor is of the centralized type at this time, the terminals of the motor winding are low, the size is small, and the cost is relatively low. When $\tau > 1$, it indicates that the winding arrangement of the motor is distributed; the terminals of the distributed winding are higher and the size is larger; under the same number of turns, it will have a higher volume and greater mass compared to the centralized winding; and the efficiency is lower. Therefore, the span of the armature winding should not be too large; K_d is the distribution factor of the winding, which will affect the size of the winding factor. In general, motors require a larger winding factor.

In order to make full use of the internal space of the rotor, the number of rotor poles should be as many as possible; however, considering the mechanical strength of the rotor, the number of rotor poles cannot be too high. Taking all the above factors into consideration and in accordance with the constraints of Equation (1), the number of rotor poles is selected as seven. For a three-phase motor, the pole–slot ratio satisfies the following formula:

$$\frac{Z}{[GCD(Z, 2p)]} = 3C \tag{2}$$

where Z is the number of stator slots, p is the number of stator pole pairs, C is a positive integer, and GCD is the greatest common divisor.

2.2. Motor Structure

According to Equation (2), it can be determined that when the number of rotor poles is selected as 14, the corresponding selectable stator slot numbers are 3, 6, 9, 12, 15, 18, 21, 24, etc. In order to achieve a higher winding factor, the difference between the number of slots and the number of poles of the motor should be as small as possible; moreover, when the number of stator slots is odd, an unbalanced magnetic force will be generated. Taking all the above factors into consideration, the final decision is to set the number of stator slots at 12. The SFM-PMIW motor shown in Figure 1 is taken as the research object, with the dimensional variables marked in structural schematic diagram. The characteristics of the motor, the mathematical modeling of multi-harmonic analysis method, and the driving operation of the motor are discussed.

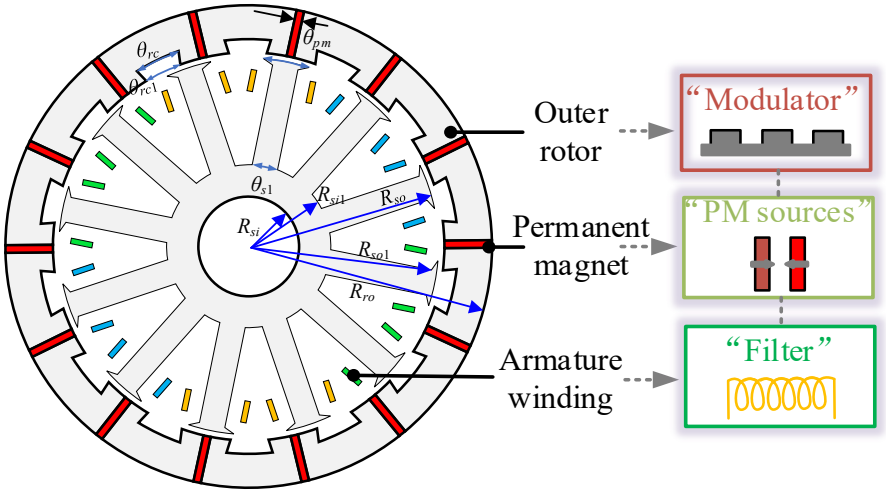


Figure 1. Initial topology diagram of the SFM-PMIW motor.

As shown in Figure 1, the rotor of the SFM-PMIW motor is placed on the outside, and the most obvious feature of the SFM-PMIW motor is the groove design on the rotor surface, which is different from the smooth surface of traditional motors, effectively improving the harmonic distribution of the air-gap magnetic field, enhancing output torque of the motor, and reducing torque ripple. In order to further achieve the design of high torque performance for the motor, next, based on the magnetic modulation mechanism, the harmonic analysis of the motor air-gap magnetic field will be conducted, and the correlation between the harmonic and the torque performance will be analyzed.

3. Analysis of Modulating Principle and Torque Generating Principle

3.1. The Generating Principle of Air-Gap Flux Density in the PM Field

For the permanent magnetic field in the SFM-PMIW motor, the rotor side where the PMs are located is the permanent magnetic source side, while the stator acts as the modulator. Based on the three elements of the magnetic field modulation motor, the generation mechanism of the PM magnetomotive force (MMF) is crucial for an in-depth analysis of the magnetic field modulation principle.

Firstly, the rotor with slotless design structure has a PM MMF waveform as shown in Figure 2a. Here, F_{PM0} is the MMF amplitude of the spoke-type motor under the slotless rotor structure, P_r is the number of pole pairs of the PM, and θ_r is the width of the rotor core. As shown in Figure 2, Fourier decomposition is performed on the radial MMF components $F_{PM0r}(\theta)$ and tangential MMF components $F_{PM0t}(\theta)$ of the PM magnetomotive force (MMF) in the slotless motor, obtaining the following expressions for the PM MMF:

$$\begin{aligned} F_{PM0r}(\theta,t) &= \sum_{i=1,3,5,\ldots}^{\infty} F_{ri}\cos(iP_r\Omega_r t + iP_r\theta + \theta_{r0}) \\ F_{PM0t}(\theta,t) &= \sum_{i=1,3,5,\ldots}^{\infty} F_{ti}\sin(iP_r\Omega_r t + iP_r\theta + \theta_{t0}) \end{aligned} \tag{3}$$

where Ω_r is the mechanical angular velocity of the rotor, while F_{ri} and F_{ti} are the i-th harmonic amplitudes of the radial and tangential PM MMF of the motor, respectively, and θ_{r0} and θ_{t0} are the i-th harmonic initial phases of the radial and tangential PM MMF of the motor; θ is the rotation angle of the air-gap.

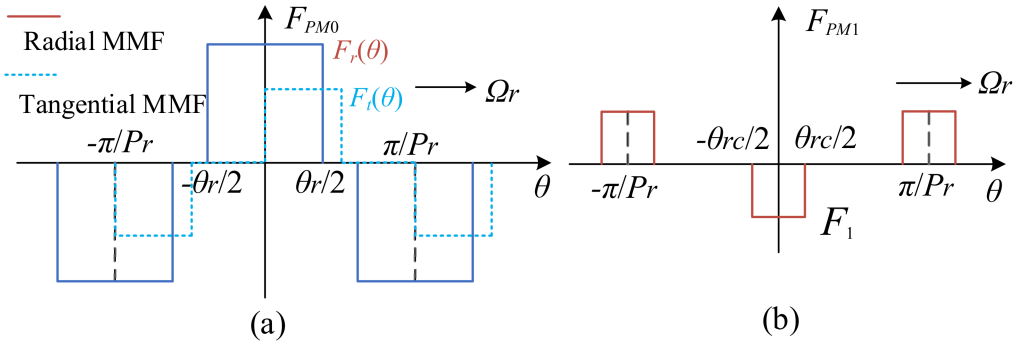


Figure 2. MMF of the SFM-PMIW motors. (**a**) Rotor-PM MMF. (**b**) MMF generated by the introduction of a rotor dummy slot.

The PM MMF waveform of the rotor slotted structure is shown in Figure 2b, F_{PM1} is the amplitude of the PM MMF introduced by the rotor slotted structure, and θ_{rc} is the rotor slot opening width. Subsequently, by performing Fourier decomposition on the PM MMF F_{PM1} function of the slotted motor, the expression for the PM MMF of the slotted motor can be derived as follows:

$$F_{PM1}(\theta, t) = \sum_{n=1}^{\infty} F_{PM1} \cos nP_r(\Omega_r t + \theta + \theta_0) \tag{4}$$

According to the design concept of the SFM-PMIW motor, the PM MMF of the SFM-PMIW motor is obtained by combining the PM MMF of the initial spoke-type motor and the MMF changes caused by rotor slotting. The final expression is as follows:

$$\begin{aligned} F_{PMr}(\theta, t) &= F_{PM0r}(\theta, t) + F_{PM1r}(\theta, t) = \sum_{i=1,3,5,\ldots}^{\infty} F_{PMri} \cos(iP_r\Omega_r t + iP_r\theta + \theta_{ri}) \\ F_{PMt}(\theta, t) &= F_{PM0t}(\theta, t) + F_{PM1t}(\theta, t) = \sum_{i=1,3,5,\ldots}^{\infty} F_{PMti} \sin(iP_r\Omega_r t + iP_r\theta + \theta_{ti}) \end{aligned} \tag{5}$$

where F_{PMri} and F_{PMti} are the amplitudes of the i-th harmonic of F_{PMr} and F_{PMt}, respectively.

Similarly, for the SFM-PMIW motor, the rotor side is a permanent magnetic source, while the stator teeth on the stator side exhibit an asynchronous modulation effect, which is expressed by the permeance of the stator core, and the stator magnetic conductance is shown in Figure 3.

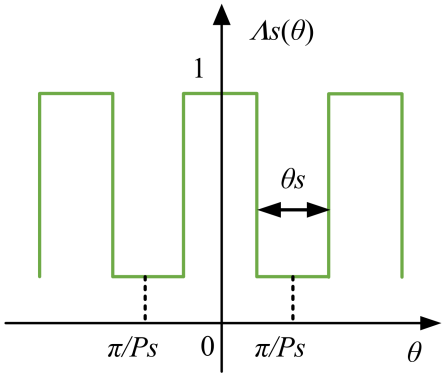


Figure 3. Permeance function of the stators in the SFM-PMIW motor.

The asynchronous permeance modulation function of the stator tooth to the rotor permanent magnetic field can be Fourier decomposed as follows:

$$\begin{aligned} \Lambda_{sr}(\theta) &= \Lambda_{sr0} + \sum_{j=1,2,\ldots}^{\infty} \Lambda_{srj} \cos(jN_s\theta) \\ \Lambda_{st}(\theta) &= \sum_{j=1,2,\ldots}^{\infty} \Lambda_{stj} \sin(jN_s\theta) \end{aligned} \tag{6}$$

where N_s is the number of modulation teeth on the stator of the motor, Λ_{sr0} and Λ_{srj} are the amplitudes of the 0-th and j-th harmonics of the stator radial permeance function, Λ_{stj} is the amplitude of the j-th harmonic of the tangential permeance function, and j is a positive integer.

Combining Equations (5) and (6), the radial and tangential flux generated by PM excitation source can be calculated, and the expressions for the corresponding radial air-gap flux density $B_{PMr}(\theta, t)$ and tangential air-gap flux density $B_{PMt}(\theta, t)$ are obtained as follows [20,21]:

$$\begin{aligned}
&B_{PMr}(\theta,t) = F_{PMr}(\theta,t)\Lambda_{sr}(\theta) + F_{PMt}(\theta,t)\Lambda_{st}(\theta)\\
&= \sum_{i=1,3,5,\ldots}^{\infty} \Lambda_{sr0}F_{PMri}\cos(iP_r\Omega_r t + iP_r\theta + \theta_{r0})\\
&+\frac{1}{2}\sum_{i=1,3,5,\ldots}^{\infty}\sum_{j=1,2,\ldots}^{\infty} F_{PMri}\Lambda_{srj}\{\cos[iP_r\Omega_r t + (iP_r + jN_s)\theta + \theta_{ri}] + \cos[iP_r\Omega_r t + (iP_r - jN_s)\theta + \theta_{ri}]\}\\
&+\frac{1}{2}\sum_{i=1,3,5,\ldots}^{\infty}\sum_{j=1,2,\ldots}^{\infty} F_{PMti}\Lambda_{stj}\{\cos[iP_r\Omega_r t + (iP_r + jN_s)\theta + \theta_{ti}] - \cos[iP_r\Omega_r t + (iP_r - jN_s)\theta + \theta_{ti}]\}
\end{aligned} \tag{7}$$

$$\begin{aligned}
&B_{PMt}(\theta,t) = F_{PMt}(\theta,t)\Lambda_{sr}(\theta) - F_{PMr}(\theta,t)\Lambda_{st}(\theta)\\
&= \sum_{i=1,3,5,\ldots}^{\infty} \Lambda_{sr0}F_{PMti}\sin(iP_r\Omega_r t + iP_r\theta + \theta_{t0})\\
&+\frac{1}{2}\sum_{i=1,3,5,\ldots}^{\infty}\sum_{j=1,2,\ldots}^{\infty} F_{PMti}\Lambda_{srj}\{\sin[iP_r\Omega_r t + (iP_r + jN_s)\theta + \theta_{ti}] + \sin[iP_r\Omega_r t + (iP_r - jN_s)\theta + \theta_{ti}]\}\\
&+\frac{1}{2}\sum_{i=1,3,5,\ldots}^{\infty}\sum_{j=1,2,\ldots}^{\infty} F_{PMri}\Lambda_{stj}\{\sin[iP_r\Omega_r t + (iP_r + jN_s)\theta + \theta_{ri}] + \sin[iP_r\Omega_r t + (iP_r - jN_s)\theta + \theta_{ri}]\}
\end{aligned}$$

From Equation (7), it can be seen that in the PM field, in addition to the fundamental wave provided by the PM excitation source, there are also a large number of harmonics of $|iP_r \pm jN_s|$ generated through asynchronous modulation by the stator modulators. Moreover, the amplitude of the motor air-gap harmonics is closely related to the geometric structure parameters of the motor.

Figure 4 shows the PM air-gap flux density and its Fourier decomposition diagram. It can be found that when the motor is under no-load condition, the seventh harmonic has the highest amplitude in the air-gap flux density generated by the permanent magnetic source, which is consistent with the number of PM pole pairs. In addition, except for the seventh harmonic amplitude, the amplitudes of the fifth and 19th harmonics are also very high. According to the $|iP_r \pm jN_s|$ order modulation behavior shown in Equation 6, the amplitudes of the modulated fifth and 19th harmonics are also very high, which is consistent with the above analysis results of the air-gap harmonic generation principle of the motor under no-load conditions, proving the reliability of the principle analysis.

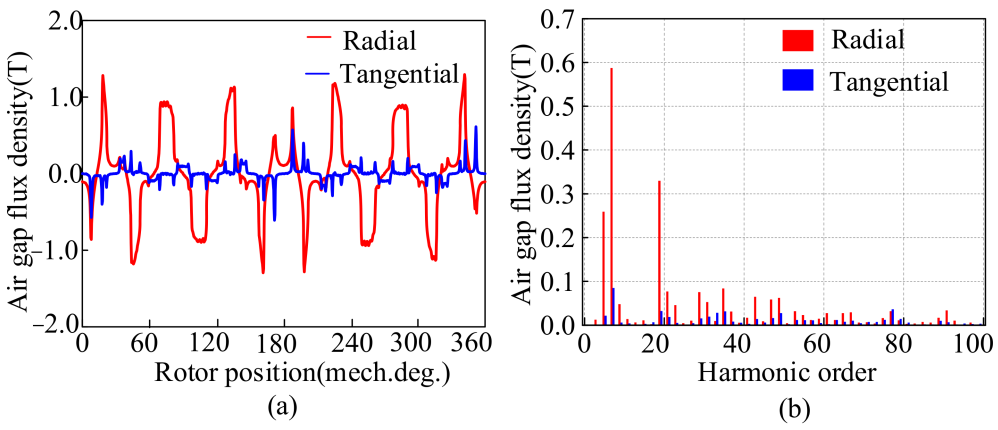


Figure 4. PM flux density and Fourier decomposition. (**a**) Waveforms. (**b**) FFT spectrum.

3.2. The Generating Principle of Air-Gap Flux Density of Armature Magnetic Field

Next, the harmonic characteristics of the armature magnetic field are analyzed, and the expression of the MMF corresponding to the three-phase windings is as follows:

$$\begin{aligned} f_A(\theta,t) &= \sum_k F_k \cos\omega t \cos k\theta \\ f_B(\theta,t) &= \sum_k F_k \cos(\omega t - 120^\circ)\cos k(\theta - 120^\circ) \\ f_B(\theta,t) &= \sum_k F_k \cos(\omega t + 120^\circ)\cos k(\theta + 120^\circ) \end{aligned} \tag{8}$$

where $\omega = \Omega_r P_r$; F_k is the amplitude of the k-th armature MMF harmonic; and the combined radial and tangential MMF of the armature magnetic field can be expressed as follows:

$$\begin{aligned} F_{Ar}(\theta,t) &= \sum_m F_{Arm}\cos(\omega t + \mathrm{sgn}(m)\cdot m\theta) \\ F_{At}(\theta,t) &= \sum_m F_{Atm}\sin(\omega t + \mathrm{sgn}(m)\cdot m\theta) \\ \mathrm{sgn}(m) &= \begin{cases} 1, m = 6k+1 \\ -1, m = 6k-1 \end{cases} \end{aligned} \tag{9}$$

where F_{Arm} and F_{Atm} are the amplitudes of the mth radial and tangential MMF harmonic of the armature magnetic field, respectively.

The asynchronous permeance distribution resulting from the slotted structure on the rotor side, which modulates the armature magnetic field, is shown in Figure 5.

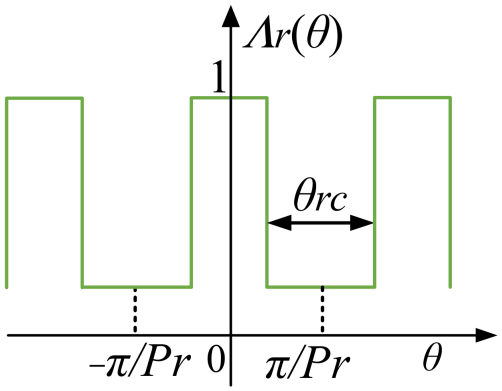


Figure 5. Rotor slotted permeance function of SFM-PMIW motor.

Performing Fourier decomposition on it can obtain the expression of the permeance modulation function caused by the slotted rotor:

$$\begin{aligned} \Lambda_{rr}(\theta,t) &= \Lambda_{rr0} + \sum_{l=1,2,\ldots}^{\infty} \Lambda_{rrl}\cos(lN_r(\theta + \Omega_r t)) \\ \Lambda_{rt}(\theta,t) &= \sum_{l=1,2,\ldots}^{\infty} \Lambda_{rtl}\sin(lN_r(\theta + \Omega_r t)) \end{aligned} \tag{10}$$

where N_s is the number of modulation teeth on the rotor of the motor, Λ_{rr0} and Λ_{rrl} are the amplitude of the 0-th and l-th harmonic of the rotor radial permeance function, Λ_{rtl} is the amplitude of the l-th harmonic of the tangential permeance function, and l is a positive integer.

$$
\begin{aligned}
&B_{Ar}(\theta,t) = F_{Ar}(\theta,t)\Lambda_{rr}(\theta,t) + F_{At}(\theta,t)\Lambda_{rt}(\theta,t)\\
&= \sum_{m}^{\infty}\Lambda_{rr0}F_{Arm}\cos(\omega t + \mathrm{sgn}(m)\cdot m\theta)\\
&+\frac{1}{2}\sum_{l}^{\infty}\sum_{m}^{\infty}F_{Arm}\Lambda_{rrl}\left\{\begin{array}{l}\cos[(1+2l)\omega t + (\mathrm{sgn}(m)\cdot m + lN_r)\theta]\\ +\cos[(1-2l)\omega t + (\mathrm{sgn}(m)\cdot m - lN_r)\theta]\end{array}\right\}\\
&+\frac{1}{2}\sum_{l}^{\infty}\sum_{m}^{\infty}F_{Atm}\Lambda_{rtl}\left\{\begin{array}{l}\cos[(1+2l)\omega t + (\mathrm{sgn}(m)\cdot m + lN_r)\theta]\\ -\cos[(1-2l)\omega t + (\mathrm{sgn}(m)\cdot m - lN_r)\theta]\end{array}\right\}\\
&B_{At}(\theta,t) = F_{At}(\theta,t)\Lambda_{rr}(\theta,t) - F_{Ar}(\theta,t)\Lambda_{rt}(\theta,t)\\
&= \sum_{m}^{\infty}\Lambda_{rr0}F_{Atm}\sin(\omega t + \mathrm{sgn}(m)\cdot m\theta)\\
&+\frac{1}{2}\sum_{l}^{\infty}\sum_{m}^{\infty}F_{Atm}\Lambda_{rtl}\left\{\begin{array}{l}\sin[(1+2l)\omega t + (\mathrm{sgn}(m)\cdot m + lN_r)\theta]\\ +\sin[(1-2l)\omega t + (\mathrm{sgn}(m)\cdot m - lN_r)\theta]\end{array}\right\}\\
&+\frac{1}{2}\sum_{l}^{\infty}\sum_{m}^{\infty}F_{Arm}\Lambda_{rrl}\left\{\begin{array}{l}\sin[(1+2l)\omega t + (\mathrm{sgn}(m)\cdot m + lN_r)\theta]\\ +\sin[(1-2l)\omega t + (\mathrm{sgn}(m)\cdot m - lN_r)\theta]\end{array}\right\}
\end{aligned}
\tag{11}
$$

As shown in Figure 6, the armature winding serves as the excitation source. According to Equation (10), the armature winding flows into the three-phase current varying both in time and space, which will generate an armature winding MMF varying in time and space on the iron core. Then, due to the permeance modulation effect of the stator tooth-slot structure and slotted rotor of the motor, an armature winding air-gap flux density varying in time and space is generated in the motor air-gap. As shown in Figure 6, the armature flux density is dominated by the fifth harmonic. According to the field-modulated motor design standard, the armature winding pole pair number $P_a = 5 = |P_r - N_s|$, verifying that the armature winding modulation behavior meets the design requirements. When the motor is under load and the armature winding serves as the excitation source, in the air-gap, apart from the fifth harmonic having the highest content, the 9th and 19th harmonics, generated by modulating the fifth armature harmonic with the cogging structure $N_r = 14$ asynchronous permeance harmonic resulting from the slotted rotor, also account for a significant proportion of the air-gap harmonics.

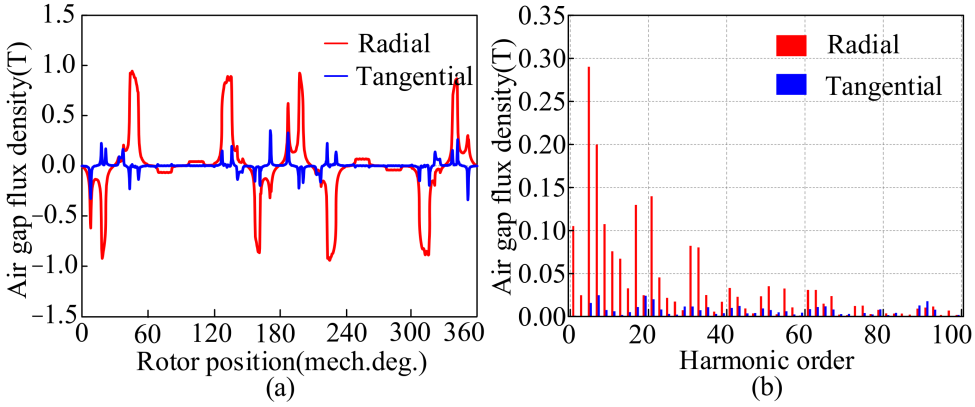


Figure 6. Armature magnetic density and Fourier decomposition. (**a**) Waveforms. (**b**) FFT spectrum.

Furthermore, when the motor is under load, the composition of the magnetic field modulation motor excitation source is divided into two parts. One is generated by the PMs, and the other is generated by the armature windings. Similarly, the modulation operator, which is one of the three elements, is also divided into two parts. They are the stator cogging and the cogging structure brought about by the slotted rotor, respectively. As shown in Figure 7, among the air-gap magnetic densities of the load motor, the fifth harmonic has the highest content. According to the design standards of the magnetic field modulation motor, the number of pole pairs of the armature winding is $P_a = 5 = |P_r - N_s|$, which indicates that the modulation behavior of the armature winding conforms to the design standards.

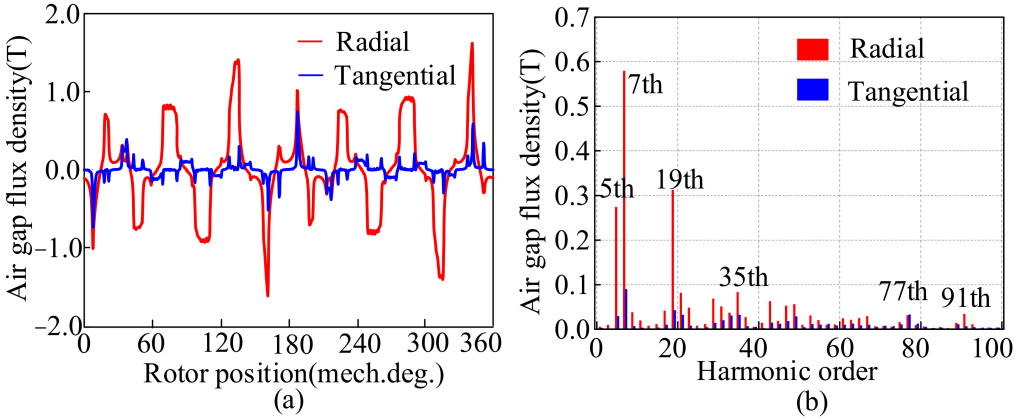


Figure 7. Air-gap flux density under the load condition and Fourier decomposition. (**a**) Waveforms. (**b**) FFT spectrum.

3.3. Analysis of Harmonic and Torque Performance

The above analysis completed the derivation process of the relationship between the air-gap flux density and harmonic components of the SFM-PMIW motor. However, different orders of harmonics have different functions in the process of energy transmission and utilization of the magnetic field. Some harmonics are closely related to the torque performance of the motor, such as output torque and torque ripple, etc. In order to study the relationship between multiple harmonics and the torque performance, the relationship between a single harmonic and the torque performance is analyzed, including the output torque and torque pulsation. The electromagnetic torque of the motor is calculated using the Maxwell stress tensor method. The calculation formula is as follows:

$$T(t) = \frac{R^2 l_{ef}}{\mu_0} \int_0^{2\pi} B_r B_t d\theta_s = \sum_i T_i \tag{12}$$

where R_g is the radius of the air-gap circumference; l_{eg} is the axial length; μ_0 is the vacuum permeability; and T_i is the torque component contributed by the i-th air-gap harmonic. By substituting the Fourier expansions of B_r and B_t into Equation (12), the calculation equation for the torque generated by each harmonic can be obtained:

$$T = \frac{\pi R^2 l_{ef}}{\mu_0} \sum_k^{\infty} \sum_{n_r}^{\infty} \sum_{n_t}^{\infty} B_{r,k,n_r} B_{t,k,n_t} \cos\{(n_t \pm n_r)\omega t + \theta_{R,k,n_r} \pm \theta_{T,k,n_t}\} \tag{13}$$

According to this equation, it can be seen that when v_r is the same as v_t, if n_r is equal to n_t, the torque expression becomes a constant; if n_r is not equal to n_t, the torque expression becomes a cosine function. Therefore, based on whether the air-gap harmonics can contribute to the electromagnetic torque and whether they can contribute to a stable output torque, the radial and tangential components of the air-gap harmonics are classified into three types of relationships: (1) The first type: The space orders v of the radial and tangential components of the air-gap harmonics are the same, and the time order n is also equal. Together, they can contribute a stable torque. (2) The second type: The space orders v of the radial and tangential components of the air-gap harmonics are the same, but the time order n is not equal. Together, they will generate torque ripple. (3) The third type: If the space orders v of the radial and tangential components of the air-gap harmonics are not the same, then the interaction between them has no effect on the electromagnetic torque.

Based on the above analysis, it can be concluded that the radial and tangential components of the harmonics have an impact on the torque performance, and the necessary condition is that their space orders are the same. That is, when $n_r = n_t$, the interaction

between B_R and B_T generates the DC component in the torque waveform. However, when n_r is not equal to n_t, the interaction between B_R and B_T forms torque ripple.

The torque of a PM motor is generally divided into three parts. The first is the cogging torque, which is directly related to the structural parameters of the motor. The second is the PM torque, which changes with the operating speed of the motor and the operating conditions. The third is the reluctance torque generated by the quadrature-axis and direct-axis inductances. The quadrature-axis and direct-axis inductances in the magnetic field modulation-type motor are close to each other, so the reluctance torque can usually be ignored. This means that the torque ripple of this type of motor basically only comes from the cogging torque when the motor is unloaded. Therefore, it is necessary to analyze the cogging torque of this motor and the harmonics associated with it.

According to Figure 8, it can be observed that the peak-to-peak value of the cogging torque of the motor is relatively high. By performing Fourier decomposition on the waveform of the cogging torque, it can be seen that the 12th harmonic is the dominant harmonic of the cogging torque. According to Equation (13), it can be inferred that the formation of the 12th harmonic component of the cogging torque mainly includes the following situations: $n_r = 1$, $n_t = 11$; $n_r = 1$, $n_t = 13$; $n_r = 3$, $n_t = 9$; or $n_r = 3$, $n_t = 15$, etc. Based on this, combined with the analysis of the time and space orders of the air-gap harmonics, the main air-gap harmonics that generate the cogging torque of the motor can be identified, thereby providing guidance for the suppression of the 12th cogging torque harmonic.

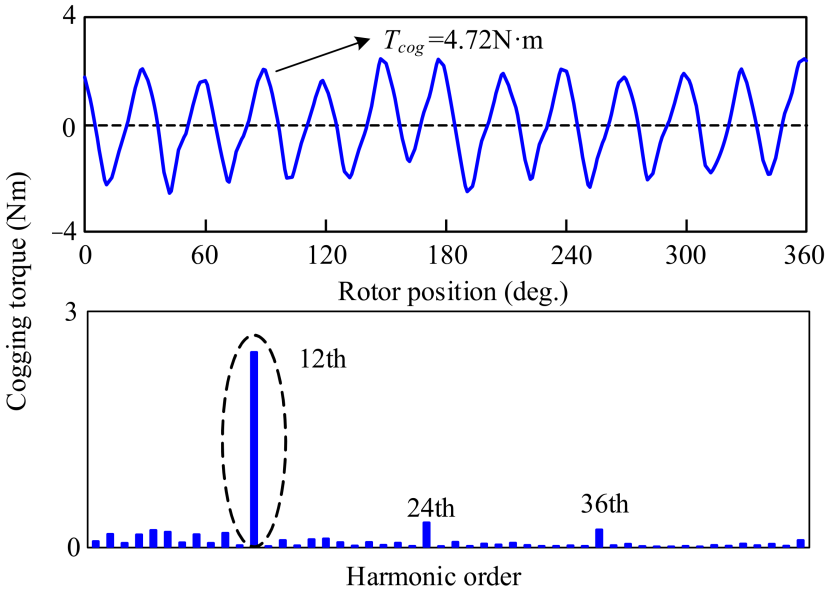


Figure 8. Cogging torque waveform and its Fourier decomposition of the initial SFM-PMIW motor.

In the proposed SFM-PMIW motor, the spectrum analysis of the air-gap harmonics related to the 12th cogging torque harmonics is shown in Table 1. It can be seen that the harmonics with $k = 35$, 77, and 91 are the main harmonics that generate the cogging torque. Additionally, during the formation of the average torque, only the harmonics with $n_r = n_t = 1$ participates. Therefore, the air-gap harmonics with $k = 35$, 77, and 91 are determined as the design targets for weakening the cogging torque in the following. This helps to suppress the cogging torque while maintaining a relatively high average torque of the motor.

Table 1. Analysis of cogging torque and air-gap harmonics of the SFM-PMIW motor.

Order	k	n_r	n_t	Contribution Degree/%
1	5	11	1	1.75
2	29	1	11	1.64
3	35	5	7	4.6
4	43	1	13	2.31
5	53	1	11	3.28
6	65	1	11	2.44
7	77	1	11	30.4
8	77	11	1	20.4
9	91	1	13	5.36
10	91	13	1	2.41
11	103	1	13	2.89
12	103	13	1	1.05

4. Harmonic Optimization Design and Performance Evaluation

4.1. Harmonic Optimization Design

Based on the foregoing analysis, the air-gap harmonics with k = 35, 77, and 91 are determined as the design targets for weakening the cogging torque. Meanwhile, the seventh harmonic as the fundamental harmonic is also selected for ensuring the electromagnetic output torque. In this section, parameter design is carried out for this motor based on finite element analysis. The parametric model is shown in Figure 9a. Meanwhile, the composition of the selected air-gap flux density harmonics is analyzed in Figure 9b.

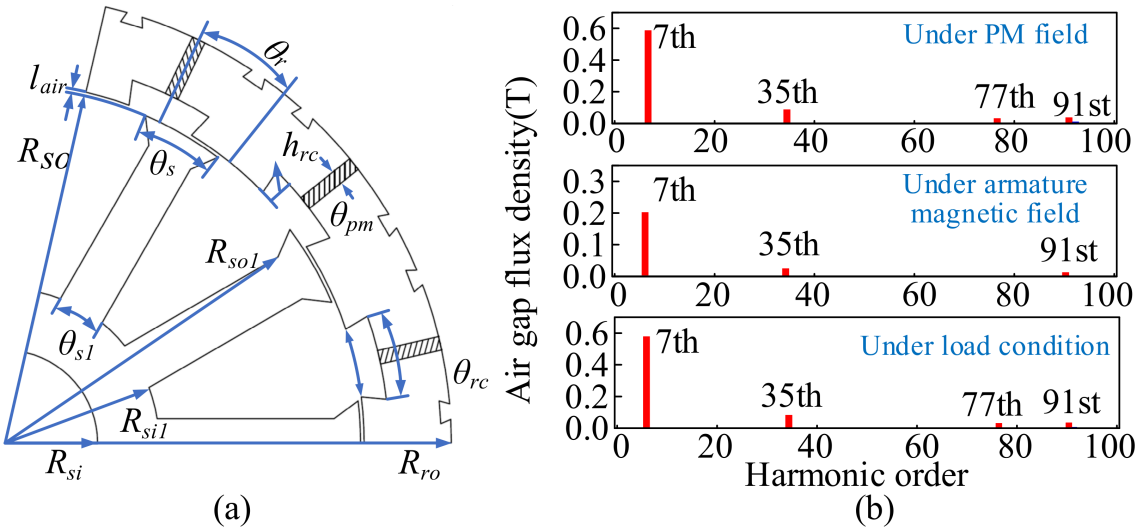


Figure 9. Main parameters and characteristic harmonic analysis of the SFM-PMIW motor. (**a**) Parameters. (**b**) The composition of the selected air-gap flux density harmonics.

The optimization process of the SFM-PMIW motor is shown in Figure 10. The parameters that need to be optimized for the motor include the top and bottom arc length of the rotor slots, the height of the rotor slots, the rotor slot offset angle, and the width of the stator teeth. The constraints for these key parameters are shown in Table 2. The main performances considered for the optimization of the motor are that of the average torque and torque ripple.

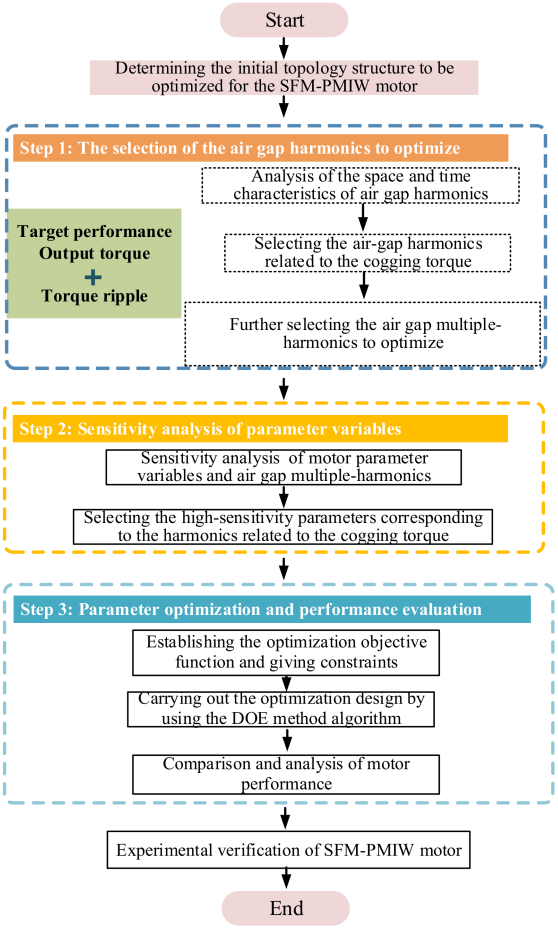


Figure 10. The flowchart of the optimization design method for the SFM-PMIW motor.

Table 2. The value range of the optimization variable of the SFM-PMIW motor.

Design Variable	Symbol	Value	Unit
Rotor slot bottom arc length	θ_{rc1}	10–12	deg
Rotor slot top arc length	θ_{rc}	11–13	deg
Rotor slot height	h_{rc}	4–5	mm
Rotor slot offset angle	θ_r	−3–3	deg
Stator tooth width	θ_{s1}	9–15	deg
Stator tooth tip width	θ_s	11–15	deg

When calculating the sensitivity of a single parameter and a single optimization objective using sensitivity analysis, the expression is as follows:

$$S(z) = Avg[S(Z_i)] = Avg\left(\frac{\left(\frac{F(z_0 \pm \Delta Z_i) - F(Z_0)}{F(Z_0)}\right)}{\left(\frac{\pm \Delta(Z_i)}{Z_0}\right)}\right) \quad (14)$$

where z is the parameter to be optimized, and z_i is the parameters listed in Table 2, namely θ_{rc1}, θ_{rc}, h_{rc}, θ_r, θ_{s1} and $thet_s$; Z_0 is the initial setting value of Z; Δz is the variation in the parameter variable z; F is the optimization objective of the sensitivity analysis; $F(z)$ is the target value when the parameter variable is z; and $Avg[S(Z_i)]$ is the arithmetic mean of $S(Z_i)$.

According to Equation (14), the sensitivity values of the parameters to be optimized for the target harmonic were obtained. The analysis result of parameter sensitivity is shown in Figure 11.

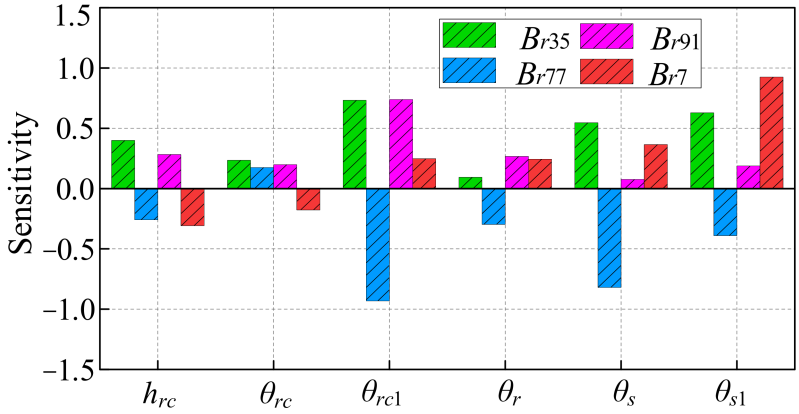


Figure 11. Analysis of parameter sensitivity.

By comparing the average sensitivity levels of the 7th, 35th, 77th and 91st harmonics for each parameter, the parameters with the higher total sensitivity are selected for further optimization. These parameters are θ_{rc1}, θ_s and θ_{s1}, respectively. Since the fundamental wave is the main harmonic order that generates torque, in the optimization design, its value should remain unchanged or increase. The 77th harmonic, which generates the main cogging torque, is given a higher weight due to its extremely significant degree of contribution to the cogging torque. As for the 35th and 91st harmonics, their importance is appropriately reduced because they have a relatively smaller impact on the cogging torque. However, they still need to be considered. This can make the optimization design results more convincing. Considering that the influence of each harmonic on the cogging torque varies, based on the contribution degree of the above main harmonics to the cogging torque, the values of the above highly sensitive parameters during the re-optimization will be combined with the contribution degree of the harmonics to the cogging torque for optimization design. On this basis, the optimal factor is defined:

$$Y_{total} = k_{Br7}\frac{B_{r7}^1}{B_{r7}^0} + k_{Br35}\frac{B_{r35}^0}{B_{r35}^1} + k_{Br77}\frac{B_{r77}^0}{B_{r77}^1} + k_{Br91}\frac{B_{r91}^0}{B_{r91}^1} \quad (15)$$

where k_{br7} is the contribution degree of the seventh harmonic to the cogging torque, k_{br35} is the contribution degree of the 35th harmonic to the cogging torque, k_{br77} is the contribution degree of the 77th harmonic to the cogging torque, and k_{br91} is the contribution degree of the 91st harmonic to the cogging torque. According to Table 2, based on the contribution degree of the main harmonics to the cogging torque, k_{br7}, k_{br35}, k_{br77} and k_{br91} are respectively set to 0.37, 0.05, 0.5 and 0.08.

As shown in Figure 12, as the bottom arc length of the rotor slotted opening increases, the amplitude of the optimal factor gradually decreases, while the influence of the stator teeth width on the optimal factor is relatively small. However, as can be seen from Figure 12a, when the stator teeth width is 6.8 deg, the optimal factor values are generally higher. From Figure 12b, it can be observed that the influence of the bottom arc length of the rotor slotted opening on the optimal factor is consistent with the law shown in Figure 12a. Therefore, the bottom arc length of the rotor slotted opening should be set at 6.49 deg. Furthermore, as shown in Figure 12b,c, the tip width of the stator teeth is approximately 8.05 deg, and the overall amplitude of the optimal factor is relatively high. Based on this, the final motor structure is determined.

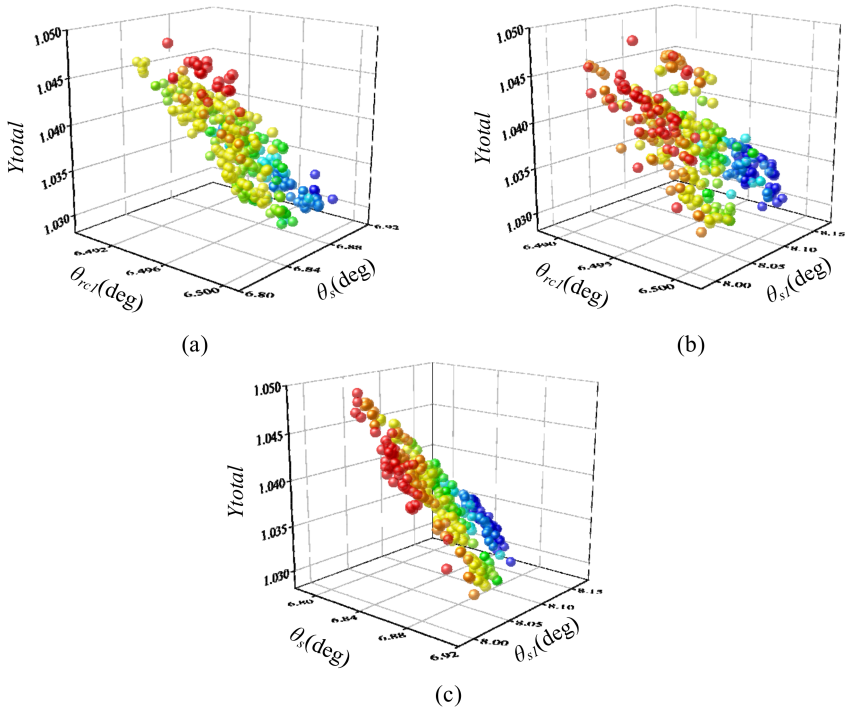


Figure 12. Influence of the main parameters on the Y_{total}. (**a**) The influence of θ_{rc1} and θ_s on the optimal factor. (**b**) The influence of θ_{rc1} and θ_s on the optimal factor. (**c**) The influence of θ_{s1} and θ_s on the optimal factor.

4.2. Performance Evaluation

To confirm the effectiveness of the design and optimization, the following will conduct an in-depth analysis and comparison of the no-load characteristics of the motor before and after optimization, such as the magnetic field distribution, no-load back electromotive force (EMF) and cogging torque, as well as the load characteristics, such as the harmonic distribution of air-gap flux density, output torque, and torque ripple, in order to prove the effectiveness of the proposed optimization method.

Figure 13 shows the distribution of the no-load magnetic field lines and the no-load flux density maps of the SFM-PMIW motor before and after optimization. As can be seen from Figure 13, the distribution of the motor magnetic field before and after parameter optimization is relatively close overall. The leakage flux phenomenon at the end of the PMs of the optimized motor has been improved. In the initial motor, more PMs are used, and although this could to some extent increase the induced electromotive force and electromagnetic torque, due to the saturation of the magnetic circuit and the increase in leakage flux, the PM utilization rate is bound to decrease. As can be seen from Figure 13b, although the total amount of rotor pole PMs has decreased, the magnetic circuit of the motor stator teeth has increased compared to the initial motor. This indicates that the effective magnetic flux in the motor remains almost unchanged despite the reduction in the PM usage. This also means that the PM magnetic source on the rotor side will have more magnetic energy that can effectively connect with the armature side, which is bound to enable a higher torque output capability and higher PM utilization rate. It can also be seen from Figure 13 that the phenomenon of relatively saturated flux density mainly occurs in the tip part of the stator teeth. After parameter optimization, the flux density on the stator teeth of the motor has been further enhanced, and the magnetic saturation phenomenon has been suppressed. This means that after optimization, the magnetic energy in the PM magnetic source of the rotor forms more effective flux through the armature winding.

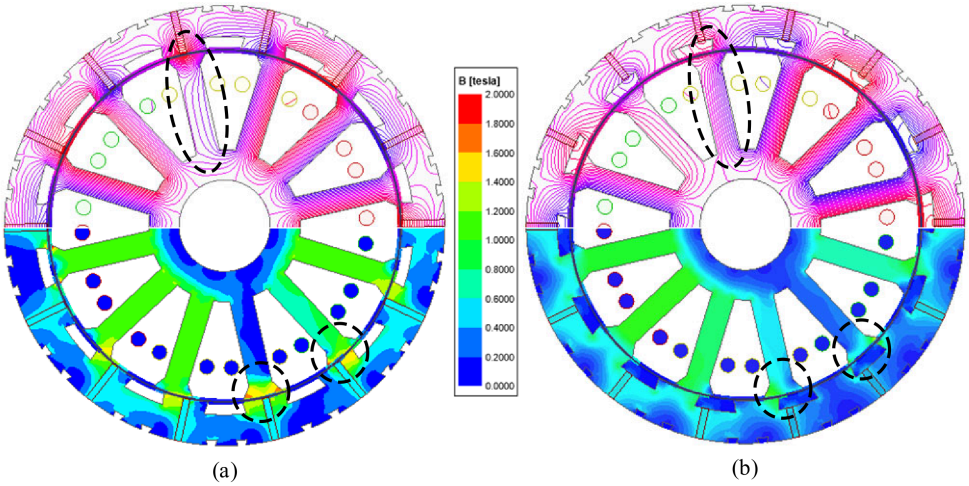


Figure 13. The magnetic field distributions and flux distributions of the SFM-PMIW motor. (**a**) Initial motor and (**b**) optimal motor.

In Figure 14, the no-load flux linkage of the motor before optimization has peak clipping, meaning that the third harmonic content in the three-phase flux linkage is relatively high. This would inevitably result in a lower sine degree of the no-load induced electromotive force. However, after the motor parameters are optimized in the previous section, the flux linkage wave presents a good sine shape, with a much higher sine degree than the initial no-load PM flux linkage in the motor. Moreover, its amplitude is higher and the effective value is larger, indicating that the utilization degree of the magnetic energy of the PM magnetic source is higher.

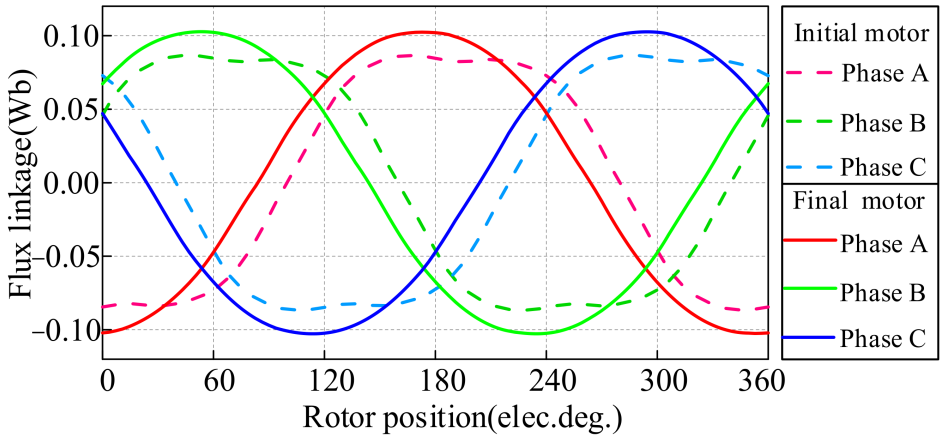


Figure 14. The flux distributions of the SFM-PMIW motor.

Figure 15 shows the three-phase no-load back electromotive force waveforms of the motor before and after optimization at the rated speed of 600 rpm. After parameter optimization, the content of high-order harmonics in the no-load back-EMF decreases, and the sine degree of the optimized back-EMF waveform becomes higher. However, after optimization, the amplitude of the induced electromotive force slightly decreases. The reason for this is the overall reduction in the PM usage. After optimization, the overall PM usage decreased by 28.2%, while the amplitude of the induced electromotive force only decreased by 11%. Therefore, the overall utilization rate of PMs in the motor has increased by 17.2%, which indicates that the motor will have better electromagnetic performance after optimization.

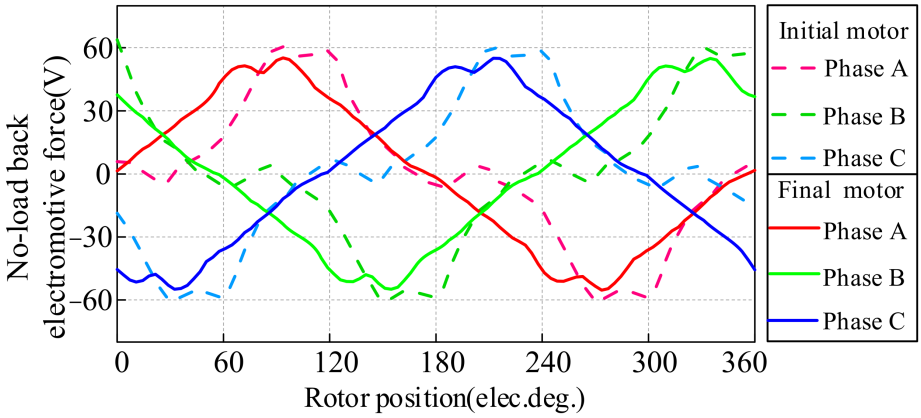


Figure 15. The back-EMF of SFM-PMIW motor before and after optimization.

Figure 16 compares the air-gap flux density and harmonic distribution of the motor before and after optimization. As shown in Figure 16a, the overall trend of the no-load air-gap flux density waveform remains unchanged after optimization. Although the PM volume is reduced, the peak values of the air-gap flux density are nearly identical to the original design, meaning the fundamental component is well preserved. Meanwhile, the optimized waveform becomes smoother, demonstrating an obvious reduction in harmonic content. Figure 16b reveals that the seventh harmonic dominates the air-gap spectrum, which matches the pole-pair number of the PMs. After optimization, the amplitude of the seventh harmonic increases, whereas the 77th harmonic responsible for major cogging torque drops substantially. The 35th and 91st harmonics, which also contribute to cogging torque, are suppressed as well. These results verify the effectiveness of the proposed optimization.

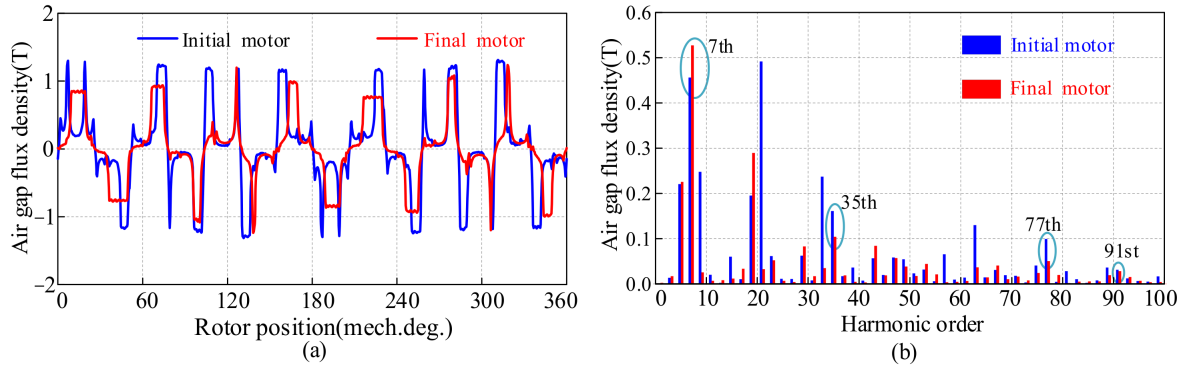


Figure 16. The airgap flux density of the SFM-PMIW motor. (**a**) Waveforms. (**b**) The distribution of the airgap flux density harmonics.

Figure 17 shows the comparison of cogging torque before and after the motor optimization. As can be seen from the figure, the cogging torque of the motor shows periodic changes both before and after the optimization, and the periodicity is obvious. This indirectly demonstrates the rationality of the analysis and the suppression of cogging torque harmonics mentioned in the previous section. Additionally, after the optimization, the cogging torque of the motor is significantly suppressed. It decreased from the initial peak-to-peak value of 4.72 Nm to 2.93 Nm, with a reduction of 38%. The 12th cogging torque decreased from 2.47 Nm to 1.43 Nm, a reduction of 42.1%.

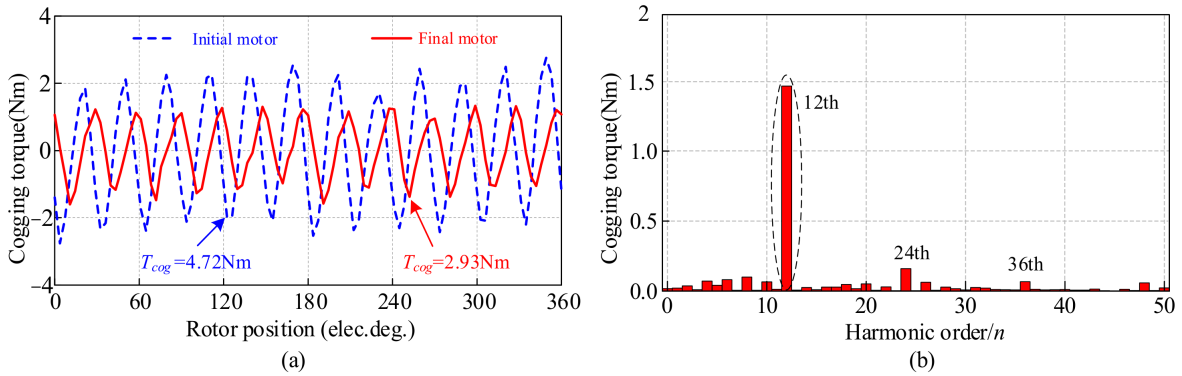


Figure 17. Comparison of cogging torque before and after optimization. (**a**) Waveforms. (**b**) FFT spectrum of the cogging torque of the final motor.

The comparison results of the torque performance of the motor before and after optimization are shown in Figure 18. The output torque has increased by 1.2 Nm, reaching 20.8 Nm. The improvement in output torque is mainly benefited by the increase in the amplitude of the seventh PM fundamental harmonic. At the same time, compared to the 25.4% torque ripple before optimization, the torque ripple after optimization has decreased to 14.8%, mainly due to the suppression of the 77th harmonic, as the cogging torque is a major source of torque ripple. The above analysis results of the torque performance confirm the analysis and discussion of the air-gap harmonics.

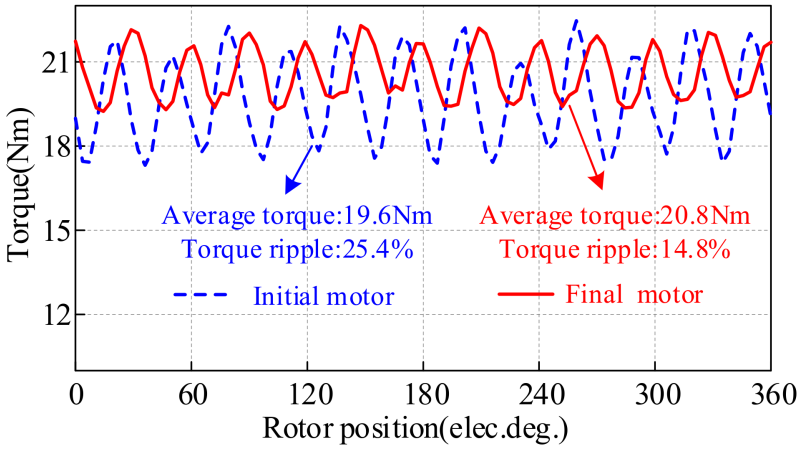


Figure 18. Comparison of torque before and after optimization.

Table 3 summarizes the performance comparison between the initial and optimal SFM-PMIW motor. After parameter optimization, the PM volume is reduced from 36.3 cm^3 to 22.9 cm^3, representing a 37% reduction in PM consumption. Meanwhile, the average torque increases from 19.6 Nm to 20.8 Nm. The cogging torque is significantly decreased from 4.7 Nm to 2.4 Nm, and the torque ripple drops to 14.8%. Benefiting from the reduced PM usage and improved output torque, the torque per PM volume rises from 0.54 Nm/cm^3 to 0.91 Nm/cm^3. In addition, the torque density increases slightly from 16.48 Nm/L to 17.49 Nm/L. The core loss decreases marginally from 19.4 W to 18.5 W. The power factor is improved from 0.82 to 0.85, and the motor efficiency rises from 81.8% to 82.6%. The results demonstrate that the proposed optimization method can effectively reduce PM consumption while maintaining and even improving the overall electromagnetic performance.

Table 3. The comparison of the performance of the SFM-PMIW motor.

Performance Index	Unit	Initial Motor	Final Motor
PM usage	cm^3	36.3	22.9
Cogging torque	Nm	4.7	2.4
Torque	Nm	19.6	20.8
Torque per PM usage	Nm/cm^3	0.54	0.91
Torque density	Nm/L	16.48	17.49
Torque ripple	-	25.4%	14.8%
Core loss	W	19.4	18.5
Power factor	-	0.82	0.85
Efficiency	-	81.8%	82.6%

5. Conclusions

This paper conducts relevant design work on the torque performance of the motor from the perspective of multiple air-gap harmonics. Guided by the principle of magnetic field modulation, a rotor-slotted spoke-type outer rotor motor is proposed for principal verification.

(1) The theoretical relationship between the air-gap harmonics and torque performance is established, and based on this, the main air-gap harmonics related to the cogging torque are identified. The 7th, 35th, 77th and 91st harmonics are selected as the optimization objectives.

(2) Then, a motor design and optimization strategy based on the characteristic harmonic weighting factor is proposed. Sensitivity analysis is adopted to screen highly influential structural parameters, and the response surface algorithm is utilized to implement parameter optimization for determining the final motor geometry.

(3) The simulation results show that each performance of the SFM-PMIW motor has been improved after optimization. With a 37% reduction in PM usage, the average torque increases by 1.2 Nm. Meanwhile, the cogging torque decreases by 50% to 2.4 Nm, and the torque ripple is reduced to 14.8%. The proposed characteristic harmonic-based optimization strategy is applicable to motors featuring rich multi-air-gap harmonics.

Author Contributions: Conceptualization, Q.L. and Z.X.; methodology, Q.L. and K.C.; software, Q.L. and K.C.; validation, Q.L., Z.X., and K.C.; formal analysis, K.C.; investigation, Q.L. and K.C.; resources, Z.X. and K.C.; data curation, K.C.; writing—original draft preparation, Q.L. and Z.X.; writing—review and editing, Q.L., Z.X., and K.C.; visualization, Q.L.; supervision, Z.X. and K.C.; project administration, Z.X. and K.C.; funding acquisition, Z.X. All authors have read and agreed to the published version of the manuscript.

Funding: This research was funded in part by the National Key Research and Development Program under Grant 2022YFB2502704, in part by the National Natural Science Foundation of China under Grant 52577056.

Data Availability Statement: The original contributions presented in this study are included in the article. Further inquiries can be directed to the corresponding author(s).

Conflicts of Interest: The authors declare no conflicts of interest.

References

1. Jiang, M.; Zhu, X.Y.; Xiang, Z.X.; Zheng, S.Y.; Fan, D.Y. Dual-sub-region rotor design of a permanent magnet hub motor with enhanced speed regulation and output torque for electric vehicles. *IEEE Trans. Ind. Electron.* **2024**, *71*, 13659–13669. [CrossRef]
2. Sun, J.L.; Wang, Z.; Ding, S.H.; Xia, J.; Xing, G.Y. Adaptive disturbance observer-based fixed time nonsingular terminal sliding mode control for path-tracking of unmanned agricultural tractors. *Biosyst. Eng.* **2024**, *246*, 96–109. [CrossRef]

3. Zhang, L.; Zhang, C.H.; Zhu, X.Y.; Li, X.Q.; Diao, X.Y.; Chen, C. Flux-intensifying design criterion and guidance of five-phase fault-tolerant in-wheel motor for distributed drive system. *IEEE Trans. Transp. Electrif.* **2026**. [CrossRef]
4. Zhu, X.K.; Liu, Y.; Li, M.; Li, R.; Zhang, Z.; Hua, W. Design, analysis and test of the dual three-phase permanent magnet vernier superconducting armature electrical machine prototype. *Supercond. Sci. Technol.* **2025**, *38*, 125031. [CrossRef]
5. Shi, Q.; Liu, D.; Mao, H.P.; Shen, B.G.; Li, M.Q. Wind-induced response of rice under the action of the downwash flow field of a multi-rotor UAV. *Biosyst. Eng.* **2021**, *203*, 60–69. [CrossRef]
6. Lu, E.; Xue, J.L.; Chen, T.T.; Jiang, S. Robust Trajectory Tracking Control of an Autonomous Tractor-Trailer Considering Model Parameter Uncertainties and Disturbances. *Agriculture* **2023**, *13*, 869. [CrossRef]
7. Xiang, Z.X.; Zhou, Y.T.; Zhu, X.Y.; Liu, Q.; Quan, L. Research on power factor enhancement of a flux-modulated PM motor utilizing a slot-space-decoupled stator shifting method. *IEEE Trans. Ind. Electron.* **2026**. [CrossRef]
8. Zhu, X.K.; Song, C.; Cheng, M.; Qin, W.; Zhao, D.; Zhang, Y.; Wang, Z. Coordinate transformation based on vector magnetic circuit theory and its application in sensorless control of SPMSM. *IEEE Trans. Ind. Electron.* **2026**, *73*, 6669–6679. [CrossRef]
9. Liu, T.; Quan, L.; Zhu, X.Y.; Fan, D.Y.; Xiang, Z.X.; Wu, R.Q. Rotor magnetic source redistribution design of a flux-controllable PM motor for vibration and noise reduction. *IEEE Trans. Transp. Electrif.* **2026**, *12*, 7976–7988. [CrossRef]
10. Li, X.L.; Wei, Z.; Zhao, Y.J.; Wang, X.S.; Hua, W. Design and analysis of surface-mounted permanent-magnet field-modulation machine for achieving high power factor. *IEEE Trans. Ind. Electron.* **2024**, *71*, 4375–4386. [CrossRef]
11. Li, X.L.; Tian, Y.C.; Dai, W.B.; Dai, J. Three-phase decoupling SVPWM based natural fault-tolerant control of six-phase vernier PM motor with open-phase fault for reducing torque ripple. *IEEE J. Emerg. Sel. Top. Power Electron.* **2026**, *14*, 411–421. [CrossRef]
12. Min, Z.Y.; Jing, L.B.; Wang, T.; Qu, R.H. A partitioned stator flux switching PM machine with strongly coupled flux reversal effect. *IEEE Trans. Transp. Electrif.* **2026**. [CrossRef]
13. Xiang, P.J.; Yan, L.; Guo, Y.M.; He, X.H.; Gerada, C.; Chen, I.M. A concentrated-flux-type PM machine with irregular magnets and iron poles. *IEEE/ASME Trans. Mechatron.* **2024**, *29*, 691–702. [CrossRef]
14. He, Z.F.; Du, Y.; Xiao, F.; Zhu, X.Y.; Chen, H.; Zhang, C. Comprehensive performance improvement of permanent magnet vernier motor for electric tractors. *IEEE Trans. Transp. Electrif.* **2024**, *10*, 4821–4832. [CrossRef]
15. Xiang, P.J.; Yan, L.; Liu, X.S.; He, X.H.; Du, N.N.; Wang, H. Structural topology design for electromagnetic performance enhancement of permanent-magnet machines. *Chin. J. Mech. Eng.* **2025**, *38*, 26. [CrossRef]
16. Sun, P.C.; Jia, S.F.; Yang, D.X.; Liang, D.W. Comparative study of novel dual winding dual magnet flux-modulated machines with different stator/rotor pole combinations. *IEEE Trans. Transp. Electrif.* **2024**, *10*, 9691–9700. [CrossRef]
17. Zhang, L.; Zhang, M.; Zhu, X.Y.; Pei, Z.F.; Chen, X. Space decoupling sensorless control of five-phase flux-intensifying PM Motor based on AFCCF-SMO considering flux-weakening operation. *IEEE. Trans. Ind. Electron.* **2025**, *72*, 6865–6875. [CrossRef]
18. Zhu, X.K.; Zhao, D.; Cheng, M.; Qin, W.; Song, C.; Wang, Z.; Hua, W. Mathematical model and vector control of SPMSM considering eddy current and hysteresis effects based on vector magnetic circuit theory. *IEEE Trans. Power Electron.* **2026**, *41*, 7383–7393. [CrossRef]
19. Fang, L.; Zhang, Y.Z.; Li, D.W.; Qu, R.H. High-torque density and low-torque ripple-oriented design method for multi-harmonics surface-mounted PM vernier machine. *IEEE Trans. Ind. Appl.* **2025**, *61*, 3687–3700. [CrossRef]
20. Li, J.Z.; Gao, Y.T.; Zha, X.M.; Hu, Z.H. Comparative study of torque production mechanism in rotor-PM and stator-PM vernier machines. *IEEE Trans. Energy Convers.* **2026**, *41*, 1780–1790. [CrossRef]
21. Li, J.Z.; Gao, Y.T.; Zha, X.M.; Hu, Z.H.; Li, G.F. Torque analysis and optimization procedure of spoke-array PM Vernier machines considering flux density harmonic contributions. *IEEE Trans. Transp. Electrif.* **2026**, *12*, 5826–5838. [CrossRef]

Disclaimer/Publisher's Note: The statements, opinions and data contained in all publications are solely those of the individual author(s) and contributor(s) and not of MDPI and/or the editor(s). MDPI and/or the editor(s) disclaim responsibility for any injury to people or property resulting from any ideas, methods, instructions or products referred to in the content.